# Coupling of phenological information and simulated vegetation index time series: Limitations and potentials for the assessment and monitoring of soil erosion risk

Markus Möller[a,*], Henning Gerstmann[b], Feng Gao[c], Thorsten Christian Dahms[d], Michael Förster[e]

[a]Martin Luther University Halle-Wittenberg, Institute of Agriculture and Nutrition Science, Farm Management Group, Karl-Freiherr-von-Fritsch-Str. 4, Halle (Saale) 06120, Germany
[b]Martin Luther University Halle-Wittenberg, Institute of Earth Sciences and Geography, Department of Remote Sensing and Cartography, Von-Seckendorff-Platz 4, Halle (Saale) 06120, Germany
[c]US Department of Agriculture, Hydrology and Remote Sensing Laboratory, Beltsville, MD 20705-2350, USA
[d]Julius Maximilians University Würzburg, Department of Remote Sensing, Oswald-Külpe-Weg 86, Würzburg 97074, Germany
[e]Technische Universität Berlin, Geoinformation in Environmental Planning Lab, Straße des 17. Juni 145, Berlin 10623, Germany

## ARTICLE INFO

## ABSTRACT

Monitoring of soils used for agriculture at frequent intervals is crucial to support decision making and refining soil policies especially in the context of climate change. Along with rainfall erosivity, soil coverage by vegetation or crop residues is the most dynamic factor affecting soil erosion. Parcel-specific soil coverage information can be derived by satellite imagery with high geometric resolution. However, their usable number is mostly, due to cloud cover, not representative for the phenological characteristics of vegetated classes. To overcome temporal constraints, spatial and temporal fusion models, such as STARFM, are increasingly applied to derive high-resolution time series of remotely sensed biophysical parameters, based on fine spatial/coarse temporal resolution imagery, such as Landsat, and coarse spatial/fine temporal resolution imagery, such as MODIS. In this context, the current study introduces an evaluation scheme for simulated vegetation index time series which enables the assessment of their performance during multiple phenological phases. The evaluation scheme is based on Germany-wide available spatial predictions of phenological phases as well as RapidEye imagery and parcel-specific crop-type information. The evaluation results show that the simulation accuracy is basically controlled by the temporal distance between MODIS and Landsat base pairs, as well as the ability of the actual Landsat image to properly represent the phenological phase of the Landsat image simulated by MODIS. In addition, we discuss the potential of simulated index times series and corresponding phenological information for the dynamic (1) definition of temporal windows where soils are potentially covered by no, sparse or dense vegetation or crop residues and (2) parameterization of soil erosion models. The database thus obtained opens up new possibilities for an efficient and dynamic erosion monitoring, which can support soil protection and hazard prevention.

© 2016 Elsevier B.V. All rights reserved.

## 1. Introduction

Soil erosion by water on agricultural land is a global phenomenon with important economic and environmental consequences, affecting soil functioning, such as biogeochemical cycling, hydrology or crop productivity (Govers et al., 2014). According to Panagos et al. (2015), the replacement cost of soil lost to water erosion in Europe can be estimated at about USD 20 billion per year.

The most important dynamic factors of soil erosion are rainfall erosivity and soil coverage by vegetation or crop residues (Panagos et al., 2014a). Since soil erosion is an event-based process and due to the spatial and temporal variability of soil erosion (Prasuhn, 2011; Evans, 2013; Aiello et al., 2015), it is a challenge to identify relevant time periods (Li et al., 2014; Alexandridis et al., 2015) with a view to predicting up-to-date *and* long-term "hotspots where serious erosion is occurring" (Boardman, 2006). Monitoring of soils affected by erosion events at frequent intervals is needed to obtain an understanding of soil erosion processes regarding land use and climate change (Evans, 2013; Prasuhn, 2011). This is crucial to support decision making and

refining soil policies (Li et al., 2014; Robinson, 2015), especially in the context of climate change (Routschek et al., 2014a,b). In Europe, this concerns regulations relating to land management practices and economic incentives, mostly in the frame of the European Union's Common Agricultural Policy (CAP; Volk et al., 2010). However, long-term monitoring of erosion features is rare due to the short-term character of low-budget research projects (Prasuhn, 2011) or due to human resource constraints within state authorities (Feldwisch, 2015).

Fig. 1 illustrates the spatiotemporal dynamic of soil coverage, which differs as a consequence of phenological development. The photograph was taken on June 19th 2013, shortly after a high-intensity rainfall event and shows two parcels with almost identical topographic and soil conditions. While the left-hand parcel is fully covered by winter wheat, the right-hand parcel is characterized by emerging maize. Due to the lack of protective cover, slope-related rills and accumulation zones of topsoil material are visible there.

During a typical vegetation cycle of crop types, the vegetation coverage is relatively low during early phenological phases, but increases until the maximum vitality of the plants is reached. Shortly after harvest, crop residue coverage is high, but decreases due to disintegration of the senescent plant components. Depending on the type of soil cultivation, soil is either not covered or (partly) protected by mulch cover.

The phenological development of crops and corresponding soil coverage information can be monitored using multi-spectral satellite imagery (de Araujo Barbosa et al., 2015). A frequently applied approach is the building of statistical models between observed soil coverages and specific multi-spectral indices (Gitelson, 2013), which result from the ratio of at least two spectral bands (Gerstmann et al., 2016b). Vegetation indices, calculated from the reflectance in the spectral wavelength range between red (*RED*) and near-infrared (*NIR*), are most sensitive to differences in fractional vegetation coverage (*FVC*) due to the abrupt reflectance rise caused by the vegetation's chlorophyll in *NIR* (Tucker, 1979). The normalized difference vegetation index (*NDVI*; Rouse et al., 1974) is the most popular vegetation index and has been found to be accurate in predicting soil coverage by green vegetation (Gitelson, 2013; Yang et al., 2013; Vrieling et al., 2008; Vrieling et al., 2014; Prabhakara et al., 2015). *NIR* and *RED* bands are also used for the detection of bare soils (BS; Cui et al., 2014; Fox et al., 2004). The estimation of crop residue coverages (*CRC*) is based on short wave infrared (*SWIR*) spectral information that is approximately 2100 nm where cellulose and lignin show a specific absorption feature (Zheng et al., 2014).

On the basis of remotely sensed and freely available imagery of coarse spatial/fine temporal resolution, such as MODIS[1] or MERIS[2], the time series of biophysical parameters enable a dynamic soil erosion risk assessment, which considers seasonal, monthly or almost weekly vegetation coverage variations on a regional or sub-continental scale (e.g., Symeonakis and Drake, 2010; Panagos et al., 2012; Guerra et al., 2014; Vrieling et al., 2014; Alexandridis et al., 2015). The monitoring of parcel-specific soil coverage information requires the operational availability of satellite imagery with fine temporal and geometric resolution, as well as with a free data distribution policy. Even though "there is currently a plethora of [optical] sensors for mapping vegetation patterns . . . " (Panagos et al., 2014b), the number of usable fine resolution imagery is mostly, due to cloud cover, not "representative for the phenological characteristics of vegetated classes" (Aiello et al., 2015). This especially concerns imagery of the Landsat family, which, for decades has offered the only data with a free distribution policy and fixed temporal repetition

(Houborg et al., 2015). However, "the sparse and unbalanced distribution of acquisition dates [... limits ...] its application in monitoring of long-term phenology change" (Tian et al., 2013).

To overcome temporal constraints, spatial and temporal fusion methods are increasingly applied to derive fine resolution time series of remotely sensed biophysical parameters. They combine coarse spatial/fine temporal and fine spatial/coarse temporal resolution imagery (Meng et al., 2013; Gao et al., 2015; Chen et al., 2015; Zhang et al., 2015). The spatial and temporal adaptive reflectance fusion model (STARFM) is one of the most widely-used spatial and temporal fusion algorithms (Gevaert and Garcia-Haro, 2015) and was developed to blend Landsat and MODIS imagery to generate synthetic Landsat surface reflectance data of fine spatial/fine temporal resolution (Gao et al., 2006). Although the STARFM is particularly considered suited to "capture reflectance changes caused by phenology" (Zhu et al., 2010), it is less appropriate when changes occur in land cover types (Huang and Zhang, 2014). The actual prediction accuracy depends on the selection of input image pairs, as well as their number and temporal distance (Olexa and Lawrence, 2014; Zhu et al., 2010). This means that the usability of simulated time series for soil coverage monitoring is restricted, since it is not known how the intra- and inter-annual dynamics of different crops can be explained by corresponding MODIS and Landsat image pairs. Thus, a thorough evaluation of the limits of the method especially in the context of agricultural settings is still needed (Lobell, 2013; Förster et al., 2015).

Regarding the example of a study site in Central Germany, this study covers three topics:

1. We show how simulated vegetation *NDVI* time series of fine temporal and geometric resolution and corresponding phenological crop information can be coupled.
2. We introduce a phenological evaluation scheme for such simulated *NDVI* time series.
3. We demonstrate how parcel-specific *NDVI* profiles can be dynamically derived for specific days of the year (DOYs) and phenological phases.

Finally, the results are discussed in the context of operational and parcel-specific assessment and monitoring of soil erosion risk by water.

## 2. Materials and methods

### 2.1. Study site

The study site is located in the German Federal State of Saxony-Anhalt approximately 30 km north of the city of Halle (Saale) (Fig. 2a and b). Due to the fertile soils of the study area (chernozems), the study site is characterized by intensive agricultural land use. The soils are at high risk of erosion because of heterogeneous landscape morphology, the erodibility of the dominant loess substrate and occurring intense rainstorm events (Möller et al., 2012). The most frequently grown crop types within the study site are winter wheat (WW; *Triticum aestivum* L.), winter barley (WB; *Secale cereale* L.), winter rapeseed (WR; *Brassica napus* L.), maize (MA; *Zea mays* L.) and common beet (CB; *Beta vulgaris*). Fig. 2c and d illustrates typical relations of crop type-specific area percentages in the study site for 2011 and 2012.

### 2.2. Data

#### 2.2.1. Landsat and MODIS

For the study area, five multi-spectral Landsat 5 TM images (DOYs 112, 128, 208, 272 and 288) and one Landsat 7 ETM+ image (DOY 232) for 2011 with a pixel size of $30 \times 30$ m$^2$ were freely downloaded

---

[1] Moderate Resolution Imaging Spectroradiometer (http://modis.gsfc.nasa.gov).
[2] MEdium Resolution Imaging Spectrometer (https://earth.esa.int/web/guest/missions/esa-operational-eo-missions/envisat/instruments/meris).

**Fig. 1.** Photograph of two parcels in Central Germany taken on June 19th 2013. The left parcel is covered by winter wheat. On the right parcel, maize emerges. Source: Photographer: Daniel Wurbs, http://www.geoflux.de.

from the USGS Earth Explorer website[3] and processed. Apart from a Landsat 5 TM image on DOY 208, all acquired images were clear over the study area. All Landsat data were atmospherically corrected using the *Landsat Ecosystem Disturbance Adaptive Processing System* (LEDAPS, Masek et al., 2006). Reflectances in *RED* and *NIR* bands were used to synthetically generate a once to twice daily time series based on the MODIS terra product MOD09GQ at $250 \times 250$ m$^2$ (Vermote et al., 2015).

The *Fmask* algorithm (Zhu and Woodcock, 2012) was used to detect clouds and cloud shadows in Landsat imagery. This algorithm has been recently improved (Zhu et al., 2015). The algorithm is publically available from the GitHub website[4]. It has been used to produce the Landsat cloud mask product by the U.S. Geological Survey (USGS) Earth Resources Observation and Science (EROS) center. All Landsat data were calibrated and atmospherically corrected using the LEDAPS approach which has been adopted by the USGS EROS center to produce the Landsat surface reflectance product. Now both Landsat surface reflectance and cloud mask are the standard Landsat data product which can be ordered and downloaded from the USGS Earth Explorer website.

The MODIS surface reflectance data product includes cloud and cloud shadow flags. We extracted the cloud and cloud shadow information from the MODIS *quality assurance* (QA) layer (i.e., the STATE_1km layer in the MOD09GA product) and generated a cloud mask file for each MODIS observation.

Clouds and cloud shadows were masked out from both Landsat and MODIS. The MODIS daily surface reflectance at $250 \times 250$ m$^2$ resolution (MOD09GQ; Vermote et al., 2015) were used to blend with Landsat surface reflectance in *RED* and *NIR* bands. *NDVI* from both actual Landsat observations and the fused Landsat-MODIS data were computed to make dense *NDVI* time-series at $30 \times 30$ m$^2$ spatial resolution.

### 2.2.2. RapidEye

Fifteen RapidEye images (see Table 3) were obtained from the RapidEye Science Archive (RESA[5]). RapidEye provides imagery at a spatial resolution $5 \times 5$ m$^2$, and across five bands that cover the *BLUE*, *GREEN*, *RED*, *REDEDGE*, and *NIR* spectral value ranges (Tyc et al., 2005). The scenes were atmospherically corrected using the *Fast Line-of-sight Atmospheric Analysis of Spectral Hypercubes* algorithm (FLAASH; Anderson et al., 2002).

Four images are affected by clouds and cloud shadows. Unlike Landsat and MODIS imagery, RapidEye imagery do not contain *SWIR* bands which are usually used to mask clouds. Here, clouds and cloud shadows were detected by a cluster analysis (Fraley and Raftery, 2002) of the parameter *BRIGHTNESS* which was calculated within the software environment eCognition (Trimble, 2011). The clustering results were visually classified.

### 2.2.3. Phenological and meteorological observations

In Germany, a phenological monitoring network consisting of around 1200 active volunteer observers is operated by the German Weather Service (*in German*: Deutscher Wetterdienst = DWD) according to standardized criteria (Kaspar et al., 2014). The irregularly distributed observers report the beginning of principle growth stages which subdivide the phenological cycle "in clearly recognizable and distinguishable longer-lasting developmental phases" (Bleiholder et al., 2001). The most common agricultural crops and their corresponding phenological phases observed in 2011 and 2012 are listed in Table 1.

### 2.2.4. Parcel boundaries and crop types

Parcels are legislative reference units for measuring soil conservation and erosion control (Volk et al., 2010). They are defined as unique in terms of growing crops and tillage operations (Möller et al., 2013). In Europe, detailed information about parcels' structure, size and crop type, which can vary annually, are stored in the European Commission's *Land Parcel Identification System* (LPIS; Inan et al., 2010, Montaghi et al., 2013). In principle, LPIS information is only publicly accessible in aggregated form and cannot be directly localized due to privacy protection (Kandziora et al., 2013). In this study, test site-specific data for 2011 and 2012 were made available for scientific research by the Ministry of Agriculture and Environment of Saxony-Anhalt.

---

[3] http://earthexplorer.usgs.gov.
[4] https://github.com/prs021/fmask.
[5] RapidEye Science Archive (https://resa.planet.com) is maintained by PLANET on behalf of the German Aerospace Center (DLR). This study was supported under project 634.

(a) Germany      (b) Study site

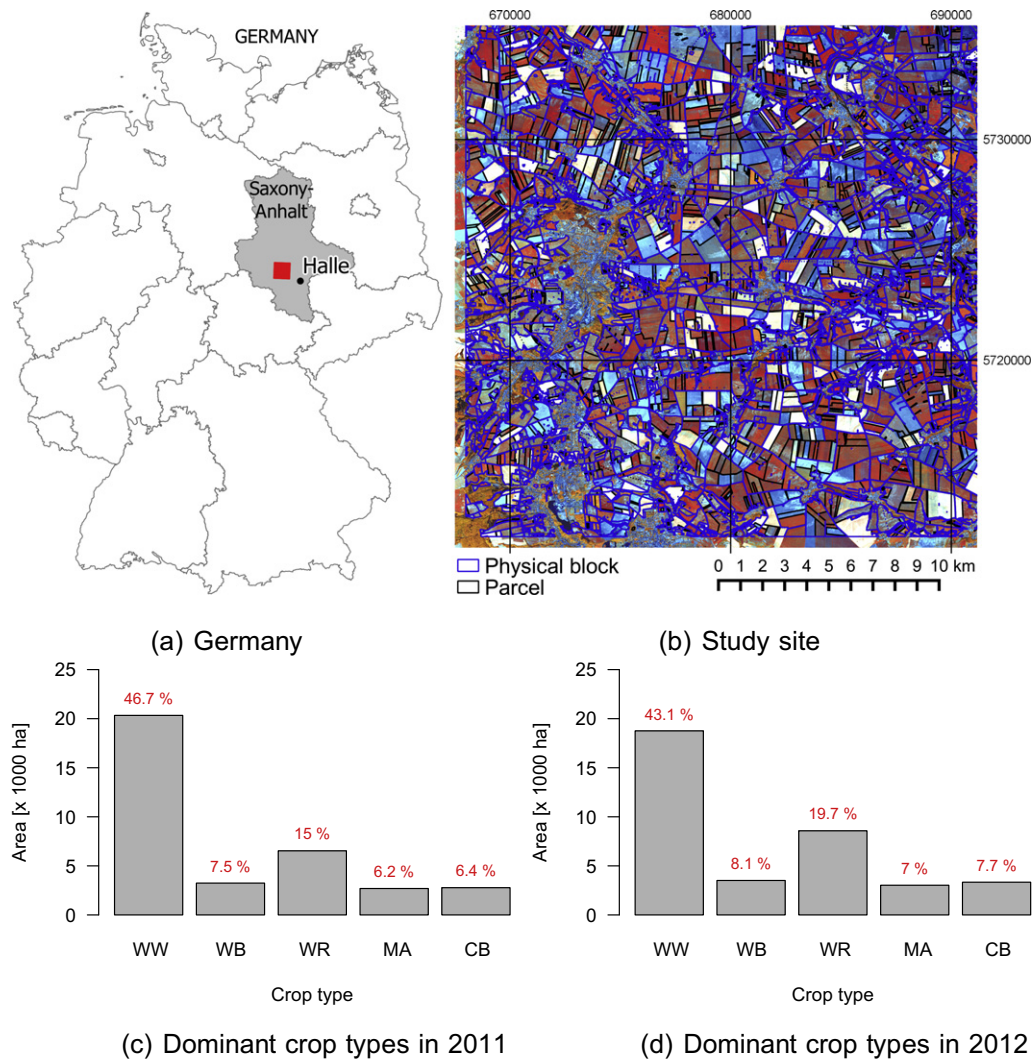(c) Dominant crop types in 2011      (d) Dominant crop types in 2012

**Fig. 2.** Saxony-Anhalt in gray and the extent of the study site in red (a), a RapidEye image (5-4-3) from May 5th 2011 overlayed with physical block and parcel polygons from 2011 (projection: EPSG code 32632; Spatialreference, 2016) b) as well as the area percentages of the most important crops winter wheat (WW), winter barley (WB), winter rapeseed (WR), maize (MA) and common beet (CB) in 2011 (c) and 2012 (d). The total agricultural used area of the study site is 43500 ha. The cultivation data were provided by the Ministry of Agriculture and Environment of Saxony-Anhalt (see Section 2.2.4). (For interpretation of the references to color in this figure legend, the reader is referred to the web version of this article.)

### 2.3. Workflow

Fig. 3 shows the technical workflow for the evaluation of a simulated index time series which can be categorized into four parts:

1. Separately for the *RED* and *NIR* spectral bands (B), reflectances of MODIS (MD) and Landsat (LS) imagery ($R_B^{MD}$, $R_B^{LS}$) are fused into synthetic spectral index images at the Landsat spatial resolution for each DOY ($I_{DOY}^{sLS}$; Section 2.3.1).

2. Germany-wide phenological information is provided by the PHASE model which enables the prediction of beginning crop-specific phenological stages by relating observed phenological events ($DOY(P)$) to measured DOY-specific mean temperatures ($T_{DOY}$) and digital elevation data ($E$; Section 2.3.2).

3. Both data sets are referred to specific reference units (RU; here: parcels) for which medians ($\bar{x}$) of simulated spectral index values for phase-specific DOY are calculated ($I_{DOY,RU}^{sLS,P}$; Section 2.3.3).

**Table 1**

List of agricultural crop types and phenological phases (Kaspar et al., 2014) observed in 2011 and 2012. 5: begin of flowering | 10: tilling, sowing, drilling | 12: emergence | 13: closed stand | 14: rosette formation | 15, 67: shooting/growth in height | 17: bud formation | 18, 66: panide emergence, beginning of ear | 19: milk ripeness | 20: wax-ripe stage | 21: yellow ripeness | 22: full ripening | 24: harvest | 41: end of flowering | 65: tassel emergence. The analyzed crop types are bold emphasized.

| Crop type (Abbreviation \| *latin name*) | ID | Phase |
|---|---|---|
| **Winter wheat** (WW \| *Triticum aestivum* L.) | **115** | 10, 12, 15, 18, 19, 21, 24 |
| Winter rye (WRy \| *Secale cereale* L.) | 121 | 10, 12, 15, 5, 18, 21, 24 |
| **Winter barley** (WB \| *Hordeum vulgare* L.) | **131** | 10, 12, 15, 18, 21, 24 |
| **Winter rapeseed** (WR \| *Brassica napus* L.) | **311** | 10, 12, 14, 67, 17, 5, 22, 24 |
| Oats (OA \| *Avena sativa* L.) | 140 | 10, 12, 15, 66, 19, 21, 24 |
| **Maize** (MA \| *Zea mays* L.) | **411** | 10, 12, 67, 5, 65, 19, 20, 21, 24 |
| Potato (PO \| *Solanum tuberosum* L.) | 612 | 10, 12, 13, 24 |
| **Common beet** (CT \| *Beta vulgaris*) | **620** | 10, 12, 13, 24 |
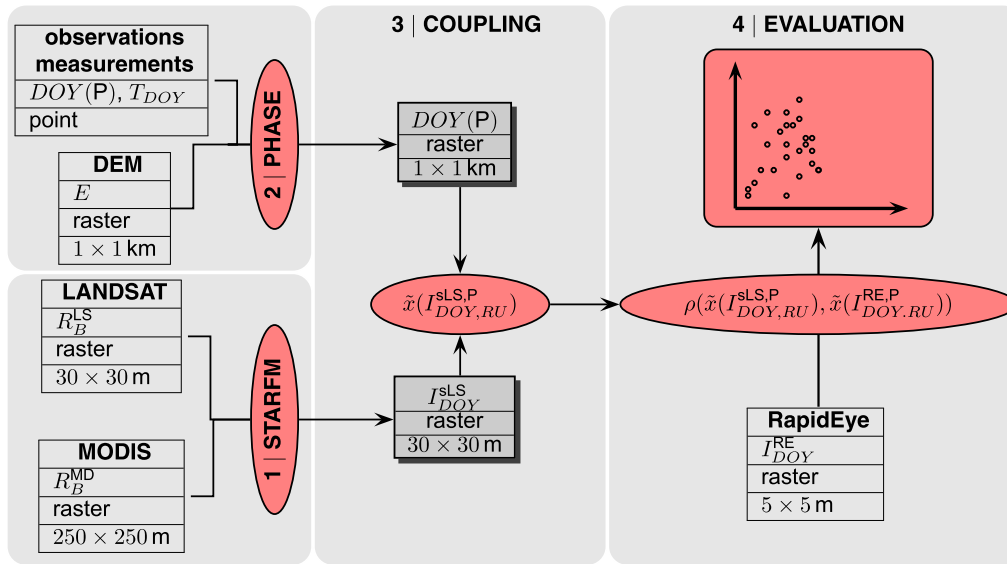
**Fig. 3.** Technical workflow for the evaluation of simulated index time series. $DOY(P)$: day of an observed phenological event | $T_{DOY}$: measured mean day-specific temperature | $E$: elevation | $R_B$: band-specific reflectance | $I_{DOY}$: DOY-specific spectral index | $\tilde{x}(I^P_{DOY,RU})$: median ($\tilde{x}$) of a spectral index $I$ for a specific DOY of an observed phenological event and a reference unit (RU).

4. During the actual evaluation process, RU-specific medians of index values of available RapidEye images ($\tilde{x}(I^{RE,P}_{DOY,RU})$) are statistically compared with medians of simulated index values ($\tilde{x}(I^{sLS,P}_{DOY,RU})$; Section 2.3.4).

The workflow is intended to be used for any spectral index. In this study, the workflow is adapted to the *NDVI*.

### 2.3.1. STARFM

The STARFM was originally introduced by Gao et al. (2006) to fuse MODIS and Landsat data to a synthetic temporal equidistant time-series with the spatial resolution of Landsat. The main objective of the STARFM was to improve the analysis of large-scale vegetation patterns (Gao et al., 2015). Other authors used the resulting synthetic imagery for crop biomass estimation (Meng et al., 2013), tracking phenological changes in dryland forest vegetation (Walker et al., 2012), supporting habitat assessment (Coops et al., 2012), analyzing forest degradation (Gärtner et al., 2016) or improving the classification of conservation tillage adoption (Watts et al., 2011). The algorithm has some restrictions, especially when predicting heterogeneous land-use pixels (Zhu et al., 2010). The accuracy of prediction depends strongly on the spatial and temporal variance of a target pixel (Emelyanova et al., 2013).

The STARFM algorithm requires a pair of images acquired on the same date (t0): one with a fine spatial resolution (most often Landsat) and one with a low spatial resolution (most often MODIS). With this basic constellation, a fine spatial resolution image on date t1 can be predicted for any given low spatial resolution image at the date t1. The basic concept is that for a homogeneous area (a pure MODIS pixel), the change of reflectance in two MODIS images (from t0 to t1) are close to the change of reflectance in Landsat images. If the changes from MODIS images are known, one can simply apply these changes to the Landsat image and predict Landsat observation at time t1. However, the difficulty is that the homogeneous pixel at coarse resolution is hard to find. To solve this problem, the STARFM algorithm uses a moving window approach to predict the central pixel by using spectrally similar pixels (e.g., similar land cover and state) to the central pixel from Landsat image at date t0. The changes

of MODIS reflectance from two dates for all spectrally similar pixels are computed within the moving window. Contribution from each spectrally similar pixel is weighted using a weighting function determined by the spatial distance from the central pixel, the spectral difference between Landsat and MODIS, and the spectral difference between two MODIS images. Once the prediction for the central pixel is determined, the algorithm moves to next pixel and assigns this pixel as the central pixel and repeats the process.

In the operational data fusion system (Gao et al., 2015), MODIS daily directional reflectances are first corrected to the nadir BRDF (Bidirectional Reflectance Distribution Function) adjusted reflectance (NBAR) using the MODIS BRDF magnitude inversion approach and MODIS BRDF parameter (Schaaf et al., 2002). The MODIS daily NBAR are reprojected and resampled to Landsat $30 \times 30$ m spatial resolution and UTM projection. Co-registration is applied to the MODIS and Landsat pair images by using Landsat image as a reference. The MODIS pair image is shifted to the location where the maximum correlation between two images occurs. The STARFM algorithm can use one or two pairs of Landsat and MODIS images to predict a Landsat-like image on a MODIS date where a Landsat overpass is not available. The one pair option is used in the operational data fusion system since it is difficult to obtain two clear Landsat-MODIS image pairs with surface conditions reasonably similar to the prediction date especially for a cloudy region.

### 2.3.2. Phenological modeling

The PHASE model was used for the generation of Germany-wide raster data sets, which contain the spatially explicit day of entry for beginning phenological crop phases (Gerstmann et al., 2016a). The statistical fitting model follows the *growing degree days* approach, which assumes a relation between the timing of observed phenological events and phase-specific thresholds of daily heat sums (Chuine et al., 2003). The model workflow consists of two steps:

1. Country-wide daily temperature observations are spatially interpolated and linked to observations representing phenological events ($DOY(P)$). Outliers, which remained after the application of automatic quality control routines by the data

set provider, are removed from the data set. This filtering procedure excludes all observations that are not inside the interval of 1.5 standard deviations around the mean of all observations. The accumulated temperature sum between sowing and the observed DOY is calculated.

2. The DOY on which the temperature sum for any location exceeds a phase-specific critical temperature sum, indicating the day of entry of the modeled phase, is finally interpolated by a Kriging algorithm.

Germany-wide available temperature and phenological stations, as well as a $1 \times 1$ km$^2$ resolution digital elevation model (DEM) were used as input data. The parameter settings used in this study are described in detail by Gerstmann et al. (2016a).

### 2.3.3. Data coupling

Table 2 illustrates a principle coupling result. Technically, RU-specific DOY and *NDVI* medians are extracted from each phenological interpolation and simulated *NDVI* layer. The period between the beginning of a certain phase and the beginning of the following phase is considered as a specific phenological phase. The corresponding phase name is then assigned to the database.

Each table element represents the state of a specific reference unit (RU) on a certain DOY, as expressed by a RU-specific median of index values and the corresponding phenological phase ($\tilde{x}(I^P_{RU,DOY})$). A column characterizes the variation of RU-specific medians in a study site on a certain DOY ($\tilde{x}(I^P_{RU\in[1...n],DOY})$). Each row stands for the RU-specific index variation during a year ($\tilde{x}(I^P_{RU,DOY\in[1...n]})$).

### 2.3.4. Evaluation

Similar to Hilker et al. (2009), Zhu et al. (2010), Walker et al. (2012) and Olexa and Lawrence (2014), synthetically generated index data set was assessed regarding their performance during multiple phenological phases by non-parametric *Spearman's rank correlation* according to Eq. (1) (Davis, 2002). The corresponding coefficient $\rho$ is an indicator of the general similarity between two sets of ranked variables. In this study, RU-specific *NDVI* medians were compared. The term inside the brackets of the numerator is the difference between the rank ($R$) of *NDVI* medians of RapidEye images ($\tilde{x}(NDVI^{RE,P}_{DOY,RU})$) and *NDVI* medians of the corresponding simulated Landsat images $\tilde{x}(NDVI^{sLS,P}_{DOY,RU})$.

$$\rho = 1 - \frac{6 \times \Sigma^n_{RU=1}\left[R\left(\tilde{x}\left(NDVI^{RE,P}_{DOY,RU}\right)\right) - R\left(\tilde{x}\left(NDVI^{sLS,P}_{DOY,RU}\right)\right)\right]^2}{n(n^2-1)} \quad (1)$$

The rank correlation was applied in order to balance possible effects on *NDVI* values as result of different data acquisition conditions (time of observation, sun angle, spectral response function, etc.) as well as of the usage of different atmospheric correction algorithms for Landsat, MODIS and RapidEye imagery (see Section 2.2; de Souza et al., 2010, López-Serrano et al., 2016).

**Table 2**
Reference unit- (RU) and phase-specific (P) medians of synthetically generated index values ($\tilde{x}(I^P_{DOY,RU})$) with RU $\in [1\ldots n]$, DOY $\in [1\ldots 365]$) and P $\in$ [5, 10, 12, 13, 15, 17, 18, 19, 20, 21, 22, 41, 65, 66, 67].

| RU | $\tilde{x}(I^P_1)$ | $\tilde{x}(I^P_2)$ | $\tilde{x}(I^P_3)$ | $\tilde{x}(I^P_{...})$ | $\tilde{x}(I^P_{365})$ |
|---|---|---|---|---|---|
| 1 | $\tilde{x}(I_{1,1})$ | $\tilde{x}(I_{2,1})$ | $\tilde{x}(I_{3,1})$ | $\tilde{x}(I_{...,1})$ | $\tilde{x}(I_{365,1})$ |
| 2 | $\tilde{x}(I_{1,2})$ | $\tilde{x}(I_{2,2})$ | $\tilde{x}(I_{3,2})$ | $\tilde{x}(I_{...,2})$ | $\tilde{x}(I_{365,2})$ |
| 3 | $\tilde{x}(I_{1,3})$ | $\tilde{x}(I_{2,3})$ | $\tilde{x}(I_{3,3})$ | $\tilde{x}(I_{...,3})$ | $\tilde{x}(I_{365,3})$ |
| ... | $\tilde{x}(I_{1,...})$ | $\tilde{x}(I_{2,...})$ | $\tilde{x}(I_{3,...})$ | $\tilde{x}(I_{...,...})$ | $\tilde{x}(I_{365,...})$ |
| n | $\tilde{x}(I_{1,n})$ | $\tilde{x}(I_{2,n})$ | $\tilde{x}(I_{3,n})$ | $\tilde{x}(I_{...,n})$ | $\tilde{x}(I_{365,n})$ |

## 3. Results

### 3.1. Simulated NDVI imagery

As a strategy to select pair dates for the STARFM, the maximum correlation of the *NDVI* bands was used based on the five Landsat 5 TM and MODIS pairs on April 22nd (DOY 112), May 8th (DOY 128), July 27th (DOY 208), September 29th (DOY 272) and October 15th (DOY 288) (see Section 2.2.1). The corresponding pixel- and DOY-specific high coefficients of determination ($R^2$) and low *RMSE* values are plotted in Fig. 4a.

The Landsat 5 TM image on DOY 208 was further improved by replacing cloud pixels using additional clear and valid Landsat 7 ETM+ pixels from DOY 232 (August 20th). The replacement was also applied to the same MODIS pixels to ensure data consistency between the Landsat and MODIS pair images.

### 3.2. Phenological phases

The interpolation results cover 33 begins of phenological phases, which are characterized by a geometric resolution of $1 \times 1$ km$^2$. In Fig. 5, the phases of WW in 2011 are exemplarily shown in order of temporal occurrence. Since emergence and sowing are strongly correlated (Gerstmann et al., 2016a), the modeling result for sowing is not displayed. The model results follow the trends, which are typical for Germany, of favored regions (e.g., the Rhine Valley, Central German Lowlands), where a phenological event occurs relatively early, and unfavored regions (e.g., coastal areas) of delayed phenology.

For each phase-specific prediction in this study, the accuracy metrics *RMSE* and $R^2$ have been calculated using 10-fold cross validation (Fig. 4b; Gerstmann et al., 2016a). Accordingly, the resulting model accuracies vary from phase to phase, but can be characterized by medians of $\tilde{x}(RMSE) = 4.6$ and $\tilde{x}(R^2) = 0.68$. The *RMSE* decreases during a vegetation cycle, beginning with an *RMSE* of approximately 11 days for *emergence* and four days for *yellow ripeness*.

### 3.3. Coupling of phenological and spectral index data

The coupling results are visualized in Figs. 6 and 7. LPIS parcel objects from 2011 have acted as RUs (see Section 2.2). For winter crops, parcel objects from 2011 and 2012 have been used, since these crop types usually change on parcels after harvest in the summer. Based on the database illustrated in Table 2 (Section 2.3.3), all crop-specific figures result from a two-step procedure:

1. The definition of phenological temporal windows is based on phase-specific boxplots for all considered phenological events (DOYs) in 2011 (Fig. 8). A phenological phase is considered as the period between the 25% quantile of a certain phase and the 25% quantile of the following phase. In doing so, temporal gaps remain. This concerns the period between harvest and phase 10 (*beginning of tilling, sowing and drilling*), which is here referred to as a pseudo phase called *after harvest* (AH). In addition, the period between the first DOY and the first observed phase of a year is named after the last observed phase in the year before.

2. For each available simulated Landsat image, simplified box-plots of $\tilde{x}(NDVI^P_{RU\in[1...n],DOY})$ distributions are calculated (see Section 2.3.3; Figs. 6 and 7). Each yellow or red dot represents a median value ($\tilde{x}$) of the $\tilde{x}(NDVI^P_{RU\in[1...n],DOY})$ distribution. The value range between the 25% and 75% quantiles is visualized by black or gray lines ($x^{25-75}$). Black lines stand for MODIS cloud coverage (CC) of maximal 50%, gray lines for cloud coverage of maximal 100%. The comparison between each times series reveals that the gray colored $\tilde{x}(NDVI^P_{RU\in[1...n],DOY})$ distributions show a higher variability than the black-colored ones

**Table 3**
Spearman's rank correlation coefficients between parcel-specific simulated Landsat and RapidEye *NDVI* values ($\rho$) for different crop types and phenological phases (P; see Table 1).

| RE | LS | ΔDOY | WW | | WB | | WR | | MA | | CB | |
|----|----|------|-----|----|-----|----|-----|----|-----|----|------|----|
| | | | $\rho$ | P | $\rho$ | P | $\rho$ | P | $\rho$ | P | $\rho$ | P |
| 66 | 112 | −46 | 0.67 | 12 | 0.68 | 12 | 0.70 | 14 | 0.31 | AH | 0.21 | AH |
| 99 | | −13 | 0.80 | 12 | 0.78 | 15 | 0.83 | 17 | 0.67 | AH | 0.47 | 10 |
| 108 | | −4 | 0.84 | 15 | 0.79 | 15 | 0.84 | 17 | 0.55 | AH | 0.49 | 10 |
| 114 | | 2 | 0.80 | 15 | 0.79 | 15 | 0.76 | 5 | 0.56 | 10 | 0.51 | 12 |
| 128 | 128 | 0 | 0.95 | 15 | 0.92 | 18 | 0.94 | 5 | 0.72 | 12 | 0.82 | 12 |
| 142 | | 14 | 0.20 | 18 | 0.05* | 18 | 0.02* | 5 | 0.24* | 12 | 0.04* | 12 |
| 157 | | 29 | 0.29 | 18 | 0.15* | 18 | 0.12* | 5 | 0.15* | 67 | 0.15* | 13 |
| 197 | 208 | −11 | 0.54 | 21 | 0.64 | AH | 0.45 | 24 | 0.44 | 65 | 0.45 | 13 |
| 238 | | 30 | 0.18 | AH | 0.03* | AH | 0.51 | 10 | 0.28 | 20 | 0.32 | 13 |
| 245 | 272 | −27 | 0.23 | AH | 0.29 | AH | 0.46 | 12 | 0.22* | 21 | 0.32 | 13 |
| 264 | | −8 | 0.59 | 10 | 0.74 | 10 | 0.29 | 14 | 0.69 | 24 | 0.62 | 13 |
| 267 | | −5 | 0.76 | 10 | 0.90 | 12 | 0.54 | 14 | 0.81 | 24 | 0.83 | 13 |
| 275 | | 3 | 0.82 | 10 | 0.94 | 12 | 0.57 | 14 | 0.81 | AH | 0.91 | 13 |
| 317 | 288 | 29 | 0.79 | 12 | 0.92 | 12 | 0.75 | 14 | 0.29 | AH | −0.03* | AH |
| 332 | | 44 | 0.75 | 12 | 0.89 | 12 | 0.69 | 14 | 0.23 | AH | −0.21* | AH |

*ΔDOY*: temporal distances between original Landsat (LS) and RapidEye imagery (RE) | AH: after harvest. *Significance level $p > 0.01$, for all other $\rho$ values: $p < 0.01$.

(Figs. 6 and 7). This is due to the fact that heavy cloud cover reduces the number of median values, which in turn can affect the $\tilde{x}(NDVI^p_{RU \in [1...n],DOY})$ distributions' characteristic.

The resulting data set enables the visualization of phenological and spectral index patterns for a specific study site and year. In principle, the coupled results support the hypothesis of a relationship between an annual vegetation index development (here: *NDVI*) and the phenology of winter and summer crops. Typically, summer crops are characterized by a single-peak greenness season and winter crops by a bimodal (two-peak) greenness season (Förster et al., 2012). The first peak, which occurs in autumn, is due to chlorophyll formation during plant emergence. The major peak for winter crops occurs in late spring. The *NDVI* peak of summer crops occurs later than the second peak of the winter crops.

Winter crops are already sown in the autumn of the year before. Winter dormancy is related to lower *NDVI* median values after crops' *emergence* (phase 12$^{WW,WR}$; see Table 1) or *rosette formation* (14$^{WR}$; Fig. 6). The early-year green phases are characterized by resuming spring growth phases, such as *shooting* (15$^{WW,WB}$) or *stem elongation* (67$^{WR}$) and *bud formation* (17$^{WR}$), resulting in increasing *NDVI*

median values. The end of these phases marks the beginning of a *NDVI* plateau, which corresponds to the phenological phases of *ear heading* (18$^{WW,WB}$) and *flowering* (5$^{WR}$). In contrast to WW and WB, the *NDVI* median values of WR begin to decrease during this phase, due to the fact that its reflectance is increasingly dominated by yellow blossoms. During the phases of *yellow ripeness* (21$^{WW,WR}$) and *full ripening* (22$^{WR}$), the declining chlorophyll activity leads to falling *NDVI* median values, which are minimal shortly after *harvest* (24$^{WW,WB,WR}$). The reflectance is then affected by crop residues and stubbles. Approximately from DOY 240 onwards, the *NDVI* median value distributions show higher variances, which may result from overlaying effects including study-specific poor simulation accuracies (Section 3.4) or the growth of weeds and volunteer grain between harvest (phase 24) and the start of soil cultivation activities (phase 10). Finally, winter crops' *emergence* is related to intense chlorophyll activity, which causes higher vegetation indices.

Before summer crops are sown in spring, the corresponding parcels are characterized by minimal *NDVI* median values. They are associated with bare soils, which is typical for the study site at that period (see Fig. 2b). This means that catch crops are usually not seeded. Apart from the fact that the vegetation emerges
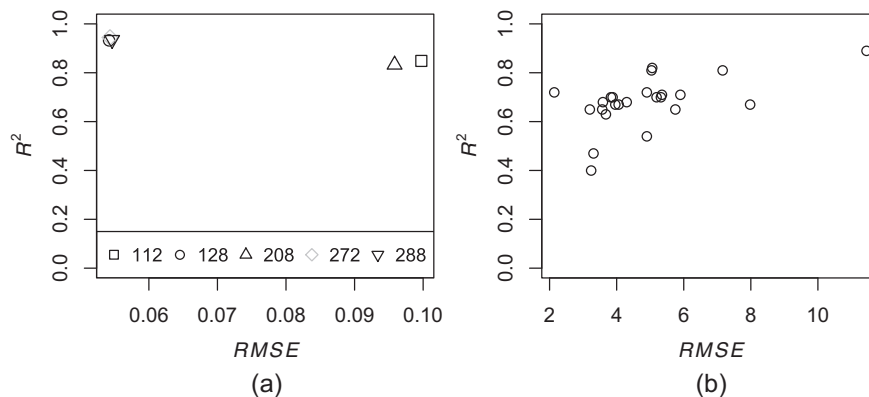


**Fig. 4.** Pixel-based internal accuracies metrics *RMSE* and $R^2$ for STARFM (a) and PHASE modeling results (b) by comparing interpolated and observed values (PHASE) respectively simulated and original Landsat *NDVI* values (STARFM).
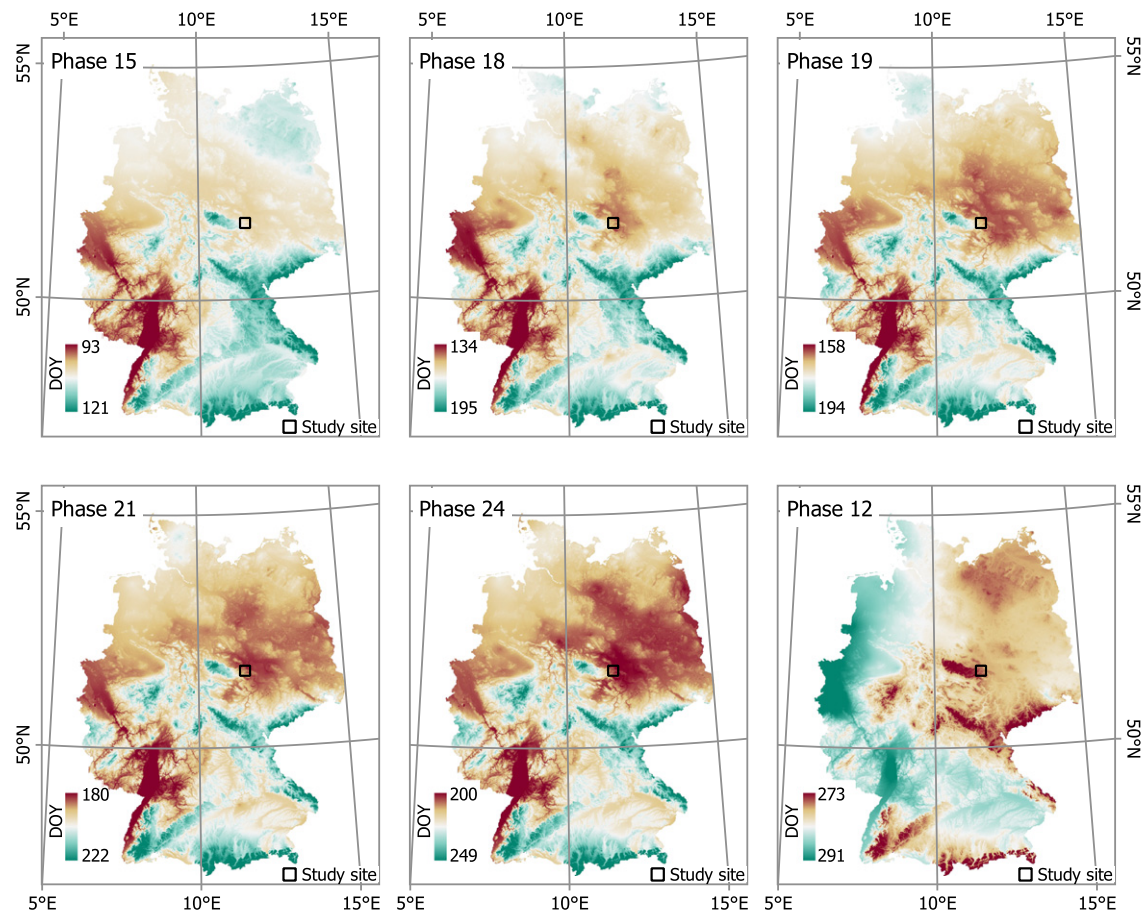
**Fig. 5.** Interpolated phenological phases *emergence* (12), *shooting* (15), *beginning of ear* (18), *milk ripeness* (19), *yellow ripeness* (21) and *harvest* (24) of winter wheat (WW) during 2011. Phase 12 (*emergence*) is part of the next vegetation cycle. Phase 10 is not displayed due to very high similarity to phase 12. (For interpretation of the references to color in this figure legend, the reader is referred to the web version of this article.)

later, the *NDVI* development is similar to winter crops. In contrast to winter crops, the *NDVI* median values increase abruptly during *emergence* ($12^{\mathrm{MA,CB}}$). Again, DOY 240 marks a boundary from where the DOY-specific *NDVI* median value variability is significantly higher.

Besides from the global statistical characterization and phenological categorization of a certain study site, the same database also enables a parcel-specific specification of parameter values regarding their

1. spatial variation on a daily basis, thereby characterizing different development stages of a phase on a certain DOY and
2. spatiotemporal variation, which depends on the phenological development of crop types.

Case 1 is illustrated by Fig. 9, which shows an unsupervised classification result (Fig. 9a), corresponding clusters and the variation of parcel-specific *NDVI* medians for WW on DOY 66 ($\tilde{x}(NDVI_{RU\in[1...n],DOY=66}^{P=12}$; Fig. 9b). According to Fig. 6a, DOY 66 is part of phase 12 (*emergence*). The study site-related median value of the $\tilde{x}(NDVI_{RU\in[1...n],DOY=66}^{P=12})$ distribution is 0.33 which indicates a low soil cover by green vegetation. The range of $\tilde{x}(NDVI)$ values is between 0 and 0.64, while the corresponding 25% and 75% quantiles are $x^{25} = 0.27$ and $x^{75} = 0.37$.

Case 2 is demonstrated by the example of the blue-marked parcel in Fig. 9a. Fig. 10a shows scatterplots of parcel-specific *NDVI* medians and corresponding DOYs for the phases of *emergence* (12), *shooting* (15) and *beginning of ear* (18) ($\tilde{x}(NDVI_{RU}^{P\in[12,15,18]})$). Accordingly, at the beginning of phase 12 between DOYs 0 and 50, $\tilde{x}(NDVI)$ values are

characterized by a large scattering. Then, DOY and $\tilde{x}(NDVI)$ values show a linear correlation. In Fig. 10b, $\tilde{x}(NDVI)$ values are summarized to phase-specific medians $\tilde{x}(\tilde{x}(NDVI_{RU}^{P}))$ of phases 12 (*emergence*), 15 (*shooting*) and 18 (*beginning of ear*).

### 3.4. Evaluation results

The evaluation results for all phases are summarized in Table 3. Apart from the *Spearman's rank correlation coefficients* between simulated Landsat and RapidEye *NDVI* median values ($\rho$), corresponding phenological phases, as well as temporal distances between acquired RapidEye and original Landsat images ($\Delta DOY$), are listed. When focusing on the temporal change in the relation between predicted and observed *NDVI* median values, it is obvious that some synthetic scenes do not fit as well as others for all crop classes and phases. In this study, this concerns DOYs 142, 157, 238 or 245. This might be due to the scene pairing. Looking at the utilized pair scenes, it can be stated for this data set that the quality of the results decreases the more the STARFM pairing date differs from the observed date (Fig. 11). Such temporal differences can lead to unrealistic synthetic images, which is related to the "temporal smoothing" effect (Zhu et al., 2010). Consequently, simulations based on the temporally close base pairs result in more accurate predictions, as is the case for DOYs 128 or 275. As other studies have already shown (e.g., Zhu et al., 2010; Walker et al., 2012; Olexa and Lawrence, 2014), the accuracy of STARFM predictions is strongly affected by the temporal gap between the base input pair and the prediction date. In
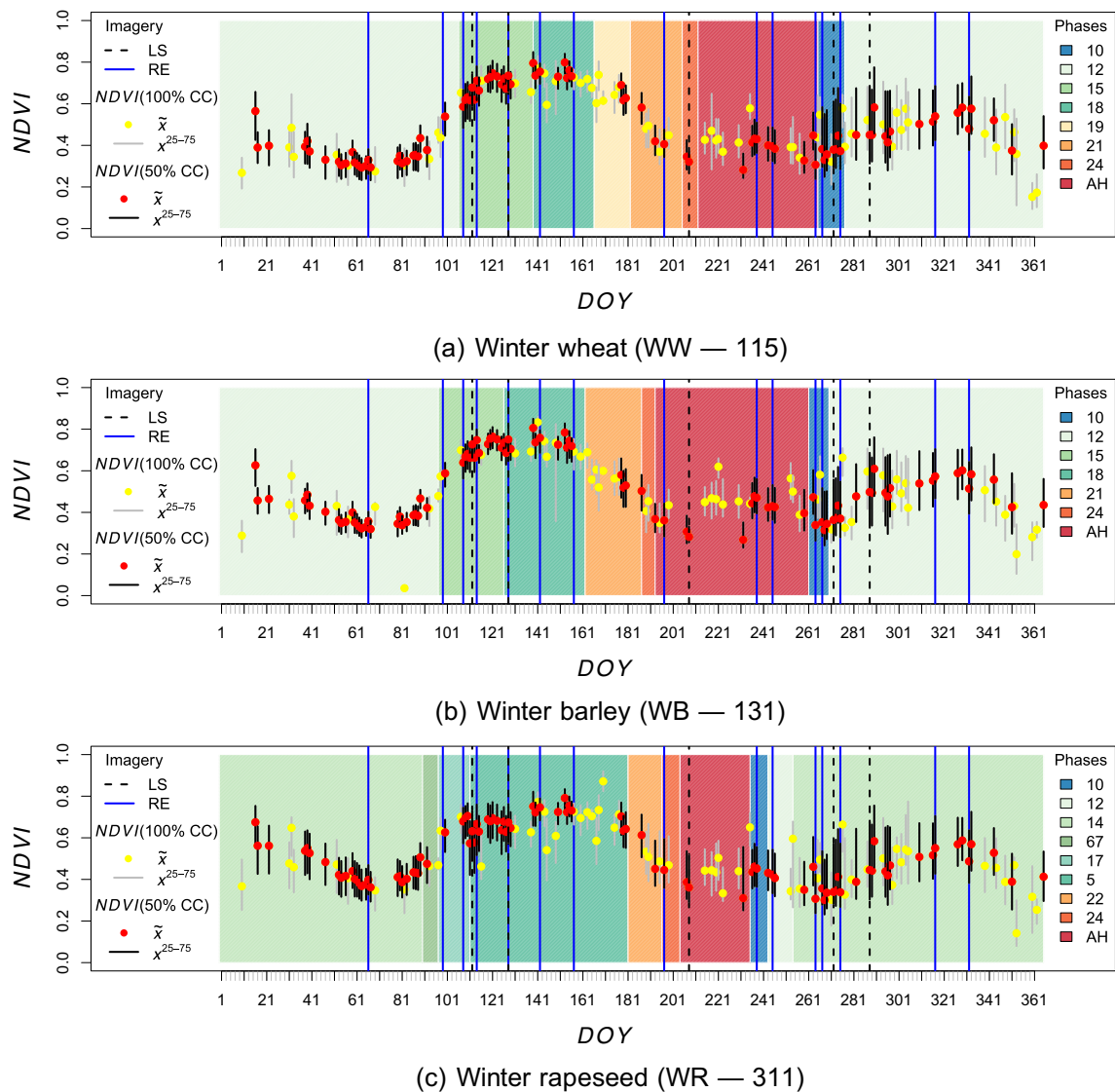
(a) Winter wheat (WW — 115)



(b) Winter barley (WB — 131)



(c) Winter rapeseed (WR — 311)

**Fig. 6.** Temporal windows of phenological phases for winter crops in 2011, corresponding DOY-specific simulated $\tilde{x}(NDVI^P_{RU\in[1...n],DOY})$ distributions for MODIS cloud coverages (CC) of maximal 50 and 100% as well as acquisition dates of RapidEye and original Landsat imagery. (For interpretation of the references to color in this figure, the reader is referred to the web version of this article.)

this study, this becomes especially clear in the example of phase 13 (*closed stand*) of CB (Fig. 11).

The additional consideration of phenological ancillary data reveals that there are phase- and crop type-specific differences, which are an expression of the temporal stability of certain phases (Fig. 11). On the one hand, high $\rho$ values have been calculated at long temporal differences for winter crop-related phases of WW and WB (*emergence*), as well as WR (*rosette formation*). Both phases are affected by winter dormancy, for instance during DOYs 66, 99, 275, 317 or 332. On the other hand, low $\rho$ values can occur close to changing phenological phases, despite close temporal distances between base pairs and prediction dates. This concerns, for instance, phase 14 (WR) on DOY 264 or phase 12 (CB) on DOY 114.

## 4. Discussion

### 4.1. Image simulation and phenology

The evaluation results in this study reflect a typical situation where the accuracy of simulated index time series is controlled by the annual changing number of base pairs for data fusion (Watts et al., 2011). In other words, the simulation accuracy is characterized by an unpredictable intra- and inter-annual change. This might be the reason why simulated index time series are currently rarely used for operational soil cover predictions and agricultural applications. It can be stated that two variables influence the quality of a synthetically derived time-series significantly:

- The pairing date of a synthetic scene should not deviate strongly from the date of interest within the time-series.
- Long phases with a stable phenological development can be predicted with higher precision (e.g., phases 12 and 14 of winter crops) than for shorter phases with rapid changes (e.g., phases 5, 12 and 13 of summer crops).

From a pragmatic point of view, phenological information, such as that provided by the PHASE model, seems to be helpful for a rapid assessment of synthetic imagery whether the number of base pairs covers time periods of seasonal changes in vegetation or crop type
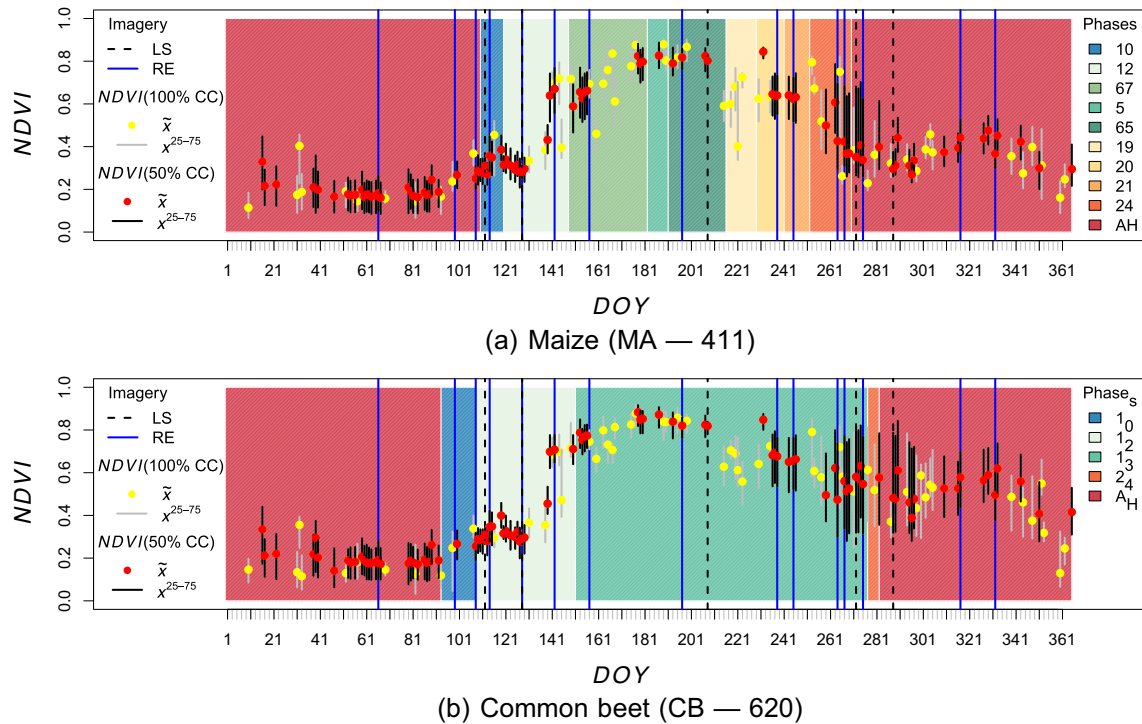
**Fig. 7.** Temporal windows of phenological phases for summer crops in 2011, corresponding DOY-specific simulated $\tilde{x}(NDVI^{P}_{RU \in [1...n],DOY})$ distributions for MODIS cloud coverages (CC) of maximal 50 and 100% as well as acquisition dates of RapidEye and original Landsat imagery. (For interpretation of the references to color in this figure, the reader is referred to the web version of this article.)

changes in a sufficient manner. For instance, the temporal gap in base pairs between DOYs 128 and 208 causes poor simulation results (Table 3). In this period, all investigated crop types are characterized by a frequent change in phenological phases (see Figs. 6 and 7).

The data situation is expected to improve when the optical multispectral sensors, such as Sentinel-2 or HJ-1, are fully operational (Drusch et al., 2012; Verrelst et al., 2012; Bian et al., 2015; Valero et al., 2016). The European Space Agency's Sentinel-2 constellation is designed to allow a temporal resolution of 10 days at the equator

with one satellite, and five days with two satellites. The HJ-1 sensor should be considered as the Chinese counterpart of Sentinel-2, with a similar temporal and geometric resolution, but fewer spectral bands and a smaller spectral range.

However, the potential high revisit frequency is limited by cloud coverage, which decreases the actual acquiring frequency of optical imagery (Valero et al., 2016; Whitcraft et al., 2015). This is especially true in temperate regions, such as Central Europe. As recently shown by Wu et al. (2015), the number of potential suitable images can be
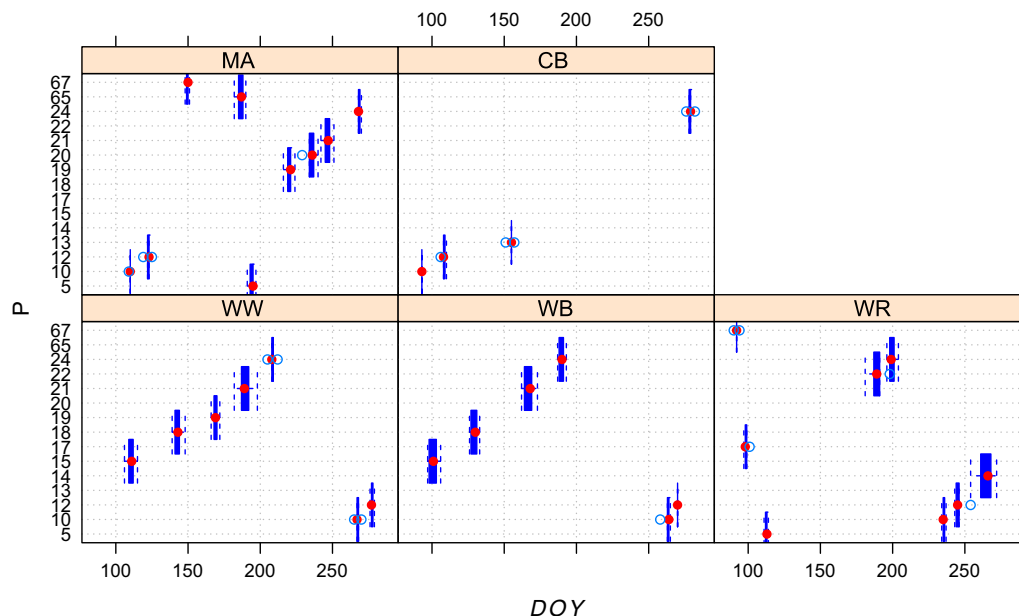


**Fig. 8.** Phase-specific (P) boxplots of predicted phenological events (DOY) for the study site in 2011 (Phase names: see Table 1).
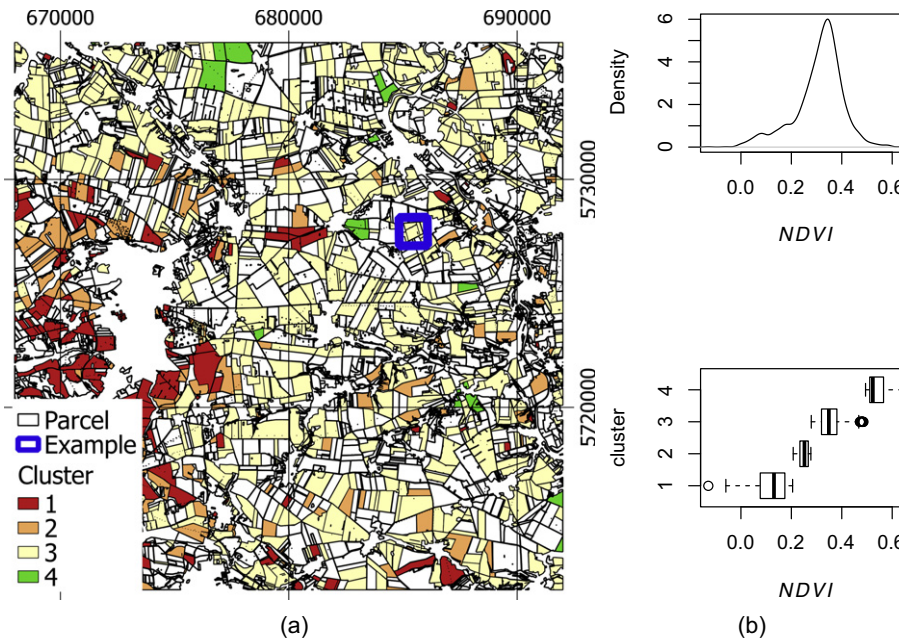
**Fig. 9.** Classification result of parcel-specific *NDVI* medians for winter wheat in 2011 and DOY 66 (a; projection: EPSG code 32632; Spatialreference, 2016), corresponding cluster and *NDVI* median distribution (b). (For interpretation of the references to color in this figure, the reader is referred to the web version of this article.)

increased by using different fine-resolution satellite imagery. But different sensor systems entail the correction of systematic biases. This can even be challenging for different Landsat sensors (Sulla-Menashe et al., 2016) and requires a lot of data processing work (Wu et al., 2015).

Nevertheless, the selection of optimal base pairs may gain in importance regarding the application of spatiotemporal fusion models. Concerning the example of HJ-1 imagery, Meng et al. (2013) have shown that crop phenology is an important parameter in the computation of time distance weights, which have to be proven as enhancements to the STARFM algorithm. Thus, "the authors recommend [. . . ] phenological information be taken as input when the algorithm is applied in operational monitoring". Here, we see a great potential of the introduced PHASE model. The thematic depth of the PHASE prediction results should be especially emphasized, as it is superior and more crop-specific compared to common phenological remote sensing-based parameters, such as green-up, onset, end and

length of the growing season (Hird and McDermid, 2009). The PHASE model also enables the prediction of anthropogenic phases, which reflect the beginning of management practices. The knowledge about such periods is assumed to be crucial for the accuracy of data fusion (Dong et al., 2016).

### 4.2. Potentials for the parcel-specific assessment and monitoring of soil erosion risk by water

Parcel- and phase-specific simulated time series of remotely sensed biophysical indices, as presented in this study, offer opportunities for both the dynamic 1. parametrization of soil erosion models and 2. monitoring of soil erosion risk:

1. Depending on their complexity and spatiotemporal scope, soil erosion models differ regarding data requirements (Volk et al., 2010). The coupling of phenological and spectral index data



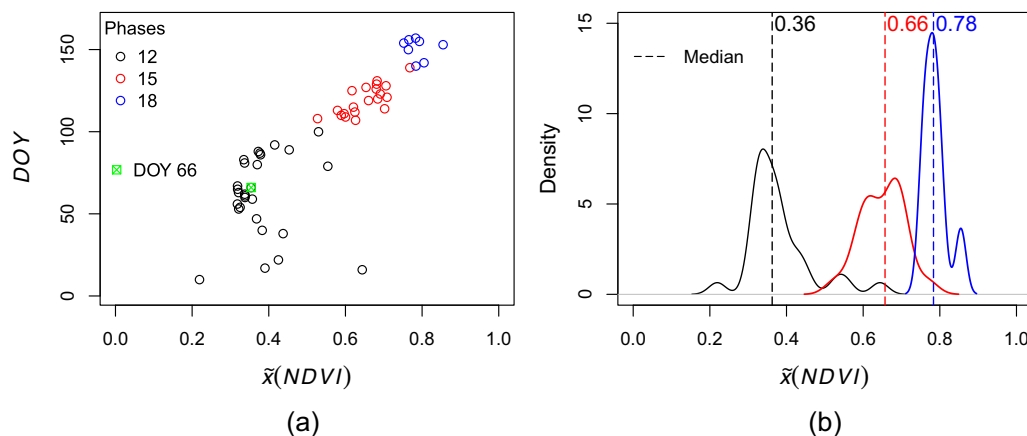**Fig. 10.** Scatter plot of *NDVI* medians and corresponding DOYs (a) as well as *NDVI* median distributions (b) for the phases *emergence* (12), *shooting* 15 and *beginning of ear* (18) for an exemplary parcel (see Fig. 9). DOY 66 is green emphasized. (For interpretation of the references to color in this figure legend, the reader is referred to the web version of this article.)
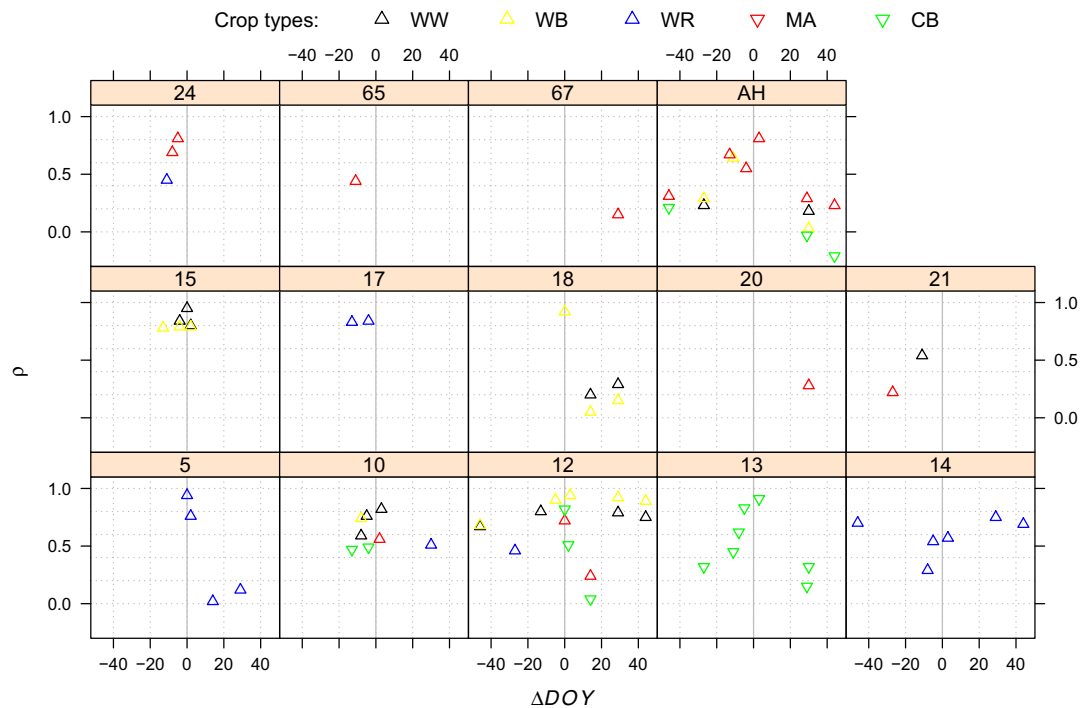
**Fig. 11.** Phase- and crop type-specific relations between *Spearman's rank correlation coefficients* (*ρ*) and temporal distances (*ΔDOY*; see Table 3).

results in a database (see Table 2 and Section 2.3.3), which enables adapted parametrization. This especially concerns the temporal resolution of information about soil coverage, which can be provided on a daily basis (see Fig. 9) or for specific periods. As shown in Fig. 10, the database enables the derivation of phase-specific soil coverage information, which can reflect intra- and inter-annual variations in a more sufficient manner than is often the case with monthly or even yearly soil coverage parameters (Vrieling et al., 2014).

2. Supposing that the abovementioned intra- and inter-annual uncertainty of simulation results (see Section 3.4) can be significantly reduced by using imagery with fine temporal and geometric resolution, such as Sentinel-2 or HJ-1 imagery, this would represent the greatest benefit of parcel- and phase-specific simulated time series in the development of automatic and (almost) real-time monitoring systems. By considering real-time areal precipitation measurements (e.g., Gerstner and Heinemann, 2008), parcels might be prioritized where soil erosion is likely to occur after heavy rain events, based on dynamic modeling results (Wenwen et al., 2012). Fischer et al. (2016) have recently shown how operationally available precipitation measurements of high spatiotemporal resolution can be used for assessing rainfall erosivity in Germany. Thus, efficient and dynamic erosion mapping could be realized (Evans, 2013) to deliver results that would "promote awareness among farmers and authorities" (Prasuhn et al., 2013). In doing so, rather passive soil protection and hazard prevention, which often only respond to apparent damages caused by single severe soil erosion events, could be overcome (e.g., Miller et al., 2012).

The usage of satellite-based indices for soil erosion modeling and monitoring requires their transformation into soil cover maps or erosion model parameters. They can be derived by applying empirical models (e.g., Van der Knijff et al., 1999). Such non-validated information is often sufficient for empirical soil erosion

models (e.g., Wischmeier and Smith, 1962; Schwertmann et al., 1990; Renard et al., 1991), which mainly aim to detect erosional patterns and their qualitative assessment. Physically based models (e.g., Roo et al., 1996; Renschler, 2003; Schindewolf and Schmidt, 2012) require quantitative information. Based on ground truth information regarding soil coverage, they can be obtained by regression equation models (e.g., Gitelson, 2013) or the application of spectral unmixing techniques (e.g., Arsenault and Bonn, 2005, de Asis and Omasa, 2007).

The *NDVI* often acts as an explaining variable, although "it cannot distinguish between bare soil and nonphotosynthetic vegetation cover, which also offers soil protection" (Vrieling et al., 2008). This means that the *NDVI* is temporally restricted during green phases, such as *emergence* or *shooting*. As already mentioned in Section 1, the identification of bare soils (Fox et al., 2004; Cui et al., 2014) or the quantification of crop residue coverage requires specific algorithms or indices, such as the *Normalized Difference Tillage Index* (*NDTI*; Zheng et al., 2014). Selection can be controlled by the integral consideration of phenological, spectral and agricultural land cover information, which allows the definition of distinct spatiotemporal scopes where different conditions of soil cover dominate (see Section 3.3).

As described in Section 2.3.3, the coupling of interpolated phenological phases (1 × 1 km$^2$) and synthetically generated *NDVI* profiles (30 × 30 m$^2$) was realized by calculating parcel-specific median values. In doing so, scale differences between both data sets ought be balanced. Since the mean parcel size of the considered crops at the study site is about 16 ha, the geometric resolution of phenological information does not fit perfectly. Thus, one subject for analysis in future is the derivation of large-scale phenological maps, which take into account their scale-specific accuracy (Möller and Volk, 2015).

The presented coupled phenological and spectral index data can help to localize "hot spot" parcels which show a potentially high risk of soil erosion on a specific date or during a specific period. In turn, a more detailed and complex modeling could be carried out in an efficient manner, since the necessary parameterization effort could be spatially restricted (Volk et al., 2010). On the one hand, this concerns the usage of fine-scale spatial objects, such as pixels or

spectral objects (Blaschke, 2010; Blaschke et al., 2014), which allow for a geometric disaggregation of parcels as well as the analysis of the within-field variability. More geometrically detailed data can be directly obtained from the simulated spectral index data or from other imagery, which is available for specific DOYs or periods. On the other hand, if ground truth information and multispectral imagery are available, *NDVI* alternatives can be calculated in an automatic manner (Rivera et al., 2014; Gerstmann et al. 2016b). In doing so, an index optimization may be carried out, resulting in a more accurate prediction of soil cover information.

## 5. Conclusion

The monitoring of parcel-specific soil erosion on farmland, together with the localization of erosional hot spots and temporal patterns, requires soil coverage information with fine spatiotemporal resolution. In this study, simulated vegetation *NDVI* time series of fine temporal and geometric resolution, derived from fused satellite MODIS and Landsat imagery, have been assessed regarding their performance during multiple phenological phases. The evaluation results show that the simulation accuracy is controlled by the temporal distance between MODIS and Landsat base pairs, as well as from the ability of the actual Landsat image to properly represent the phenological phase of the Landsat image simulated by MODIS. We consider the intra- and inter-annual uncertainty of simulation results to be a decisive factor in the general use of such data, in the context of soil erosion modeling. However, the situation is expected to improve considerably when, in addition to Landsat, satellites with higher repetition rates, such as Sentinel-2 or HJ-1, are fully operational.

On the example of a test site and one parcel, we demonstrated that simulated *NDVI* time series and corresponding phenological information enable the derivation of (1.) soil coverage information on a almost daily basis as well as (2.) phase-specific soil coverage information. The database thus obtained opens up new possibilities for an efficient and dynamic erosion monitoring, which can support soil protection and hazard prevention.

## 6. Funding

## Acknowledgments

## References

Aiello, A., Adamo, M., Canora, F., 2015. Remote sensing and GIS to assess soil erosion with RUSLE3D and USPED at river basin scale in southern Italy. CATENA 131, 174–185.

Alexandridis, T.K., Sotiropoulou, A.M., Bilas, G., Karapetsas, N., Silleos, N.G., 2015. The effects of seasonality in estimating the C-factor of soil erosion studies. Land Degrad. Dev. 26 (6), 596–603.

Anderson, G., Felde, G., Hoke, M., Ratkowski, A., Cooley, T., Chetwynd, J., Jr, Gardner, J., Adler-Golden, S., Matthew, M., Berk, A., Bernstein, L., Acharya, P., Miller, D., Lewis, P., 2002. MODTRAN4-based atmospheric correction algorithm: FLAASH (Fast Line-of-sight Atmospheric Analysis of Spectral Hypercubes). AeroSense 2002. International Society for 650 Optics and Photonics. pp. 65–71.

Arsenault, E., Bonn, F., 2005. Evaluation of soil erosion protective cover by crop residues using vegetation indices and spectral mixture analysis of multispectral and hyperspectral data. CATENA 62, 157–172. Surface characterisation for soil erosion forecasting.

Bian, J., Li, A., Wang, Q., Huang, C., 2015. Development of dense time series 30-m image products from the Chinese HJ-1A/B constellation: a case study in Zoige Plateau, China. Remote Sens. 7 (12), 16647–16671.

Blaschke, T., 2010. Object based image analysis for remote sensing. ISPRS J. Photogramm. Remote Sens. 65 (1), 2–16.

Blaschke, T., Hay, G., Kelly, M., Lang, S., Hofmann, P., Addink, E., Feitosa, R., van der Meer, F., van der Werff, H., van Coillie, F., Tiede, D., 2014. Geographic object-based image analysis - towards a new paradigm. ISPRS J. Photogramm. Remote Sens. 87, 180–191.

Bleiholder, H., Weber, E., Feller, C., Hess, M., Wicke, H., Meier, U., van den Boom, T., Lancashire, P., Buhr, L., Hack, H., Hack, H., Stauss, R., 2001. Growth stages of mono- and dicotyledonous plants. Tech. Rep. Federal Biological Research Centre for Agriculture and Forestry, Brunswick, Germany.

Boardman, J., 2006. Soil erosion science: reflections on the limitations of current approaches. CATENA 68, 73–86.

Chen, B., Huang, B., Xu, B., 2015. Comparison of spatiotemporal fusion models: a review. Remote Sens. 7 (2), 1798.

Chuine, I., Kramer, K., Hänninen, H., 2003. Plant development models. Vol. 39 of Tasks for Vegetation Science, Kluwer Academic Publishers, Dordrecht, The Netherlands., pp. 217–235. Ch. 4.1

Coops, N., Hilker, T., Bater, C., Wulder, M., Nielsen, S., McDermid, G., Stenhouse, G., 2012. Linking ground-based to satellite-derived phenological metrics in support of habitat assessment. Remote Sens. Lett. 3 (3), 191–200.

Cui, S., Rajan, N., Maas, S.J., Youn, E., 2014. An automated soil line identification method using relevance vector machine. Remote Sens. Lett. 5 (2), 175–184.

Davis, J., 2002. Statistics and Data Analysis in Geology. John Wiley & Sons.

de Araujo Barbosa, C.C., Atkinson, P.M., Dearing, J.A., 2015. Remote sensing of ecosystem services: a systematic review. Ecol. Indic. 52, 430–443.

de Asis, A.M., Omasa, K., 2007. Estimation of vegetation parameter for modeling soil erosion using linear spectral mixture analysis of Landsat ETM data. ISPRS J. Photogramm. Remote Sens. 62 (4), 309–324.

de Souza, E., Scharf, P., Sudduth, K., 2010. Sun position and cloud effects on reflectance and vegetation indices of corn. Agron. J. 102 (2), 734–744.

Dong, T., Liu, J., Qian, B., Zhao, T., Jing, Q., Geng, X., Wang, J., Huffman, T., Shang, J., 2016. Estimating winter wheat biomass by assimilating leaf area index derived from fusion of Landsat-8 and MODIS data. Int. J. Appl. Earth Obs. Geoinf. 49, 63–74.

Drusch, M., Bello, U.D., Carlier, S., Colin, O., Fernandez, V., Gascon, F., Hoersch, B., Isola, C., Laberinti, P., Martimort, P., Meygret, A., Spoto, F., Sy, O., Marchese, F., Bargellini, P., 2012. Sentinel-2: ESA's optical high-resolution mission for GMES operational services. Remote Sens. Environ. 120, 25–36.

Emelyanova, I., McVicar, T., Niel, T.V., Li, L., van Dijk, A., 2013. Assessing the accuracy of blending Landsat-MODIS surface reflectances in two landscapes with contrasting spatial and temporal dynamics: a framework for algorithm selection. Remote Sens. Environ. 133, 193–209.

Evans, R., 2013. Assessment and monitoring of accelerated water erosion of cultivated land - when will reality be acknowledged? Soil Use Manag. 29 (1), 105–118.

Feldwisch, N., 2015. Novellierung der BBodSchV - Anforderungen des vorsorgenden physikalischen Bodenschutzes. Bodenschutz 15 (4), 116–119.

Fischer, F., Hauck, J., Brandhuber, R., Weigl, E., Maier, H., Auerswald, K., 2016. Spatio-temporal variability of erosivity estimated from highly resolved and adjusted radar rain data (RADOLAN). Agric. For. Meteorol. 223, 72–80.

Förster, M., Schmidt, T., Gärtner, P., Kleinschmit, B., Gao, F., Möller, M., 2015. Evaluating the temporal stability of synthetically generated time-series for crop types in central Germany. 8th International Workshop on the Analysis of Multitemporal Remote Sensing Images (Multi-Temp).

Förster, S., Kaden, K., Förster, M., Itzerott, S., 2012. Crop type mapping using spectral-temporal profiles and phenological information. Comput. Electron. Agric. 89, 30–40.

Fox, G., Sabbagh, G., Searcy, S., Yang, C., 2004. An automated soil line identification routine for remotely sensed images. Soil Sci. Soc. Am. J. 8, 1326–1331.

Fraley, C., Raftery, A., 2002. Model-based clustering, discriminant analysis and density estimation. J. Am. Stat. Assoc. 97, 611–631.

Gao, F., Hilker, T., Zhu, X., Anderson, M., Masek, J., Wang, P., Yang, Y., 2015. Fusing Landsat and MODIS data for vegetation monitoring. IEEE Geosci. Remote Sens. Mag. 3, 47–60.

Gao, F., Masek, J., Schwaller, M., Hall, F., 2006. On the blending of the Landsat and MODIS surface reflectance: predicting daily Landsat surface reflectance. IEEE Trans. Geosci. Remote Sens. 44, 2207–2218.

Gärtner, P., Förster, M., Kleinschmit, B., 2016. The benefit of synthetically generated RapidEye and Landsat 8 data fusion time series for riparian forest disturbance monitoring. Remote Sens. Environ. 177, 237–247.

Gerstmann, H., Doktor, D., Gläßer, C., Möller, M., 2016a. Phase: a geostatistical model for the kriging-based spatial prediction of crop phenology using public phenological and climatological observations. Comput. Electron. Agric. 127, 726–738.

Gerstmann, H., Möller, M., Gläßer, C., 2016b. Optimization of spectral indices and long-term separability analysis for classification of cereal crops using multispectral rapideye imagery. Int. J. Appl. Earth Obs. Geoinf. 52, 115–125.

Gerstner, E.-M., Heinemann, G., 2008. Real-time areal precipitation determination from radar by means of statistical objective analysis. J. Hydrol. 352, 296–308.

Gevaert, C.M., Garcia-Haro, F.J., 2015. A comparison of STARFM and an unmixing-based algorithm for Landsat and MODIS data fusion. Remote Sens. Environ. 156, 34–44.

Gitelson, A., 2013. Remote estimation of crop fractional vegetation cover: the use of noise equivalent as an indicator of performance of vegetation indices. Int. J. Remote Sens. 34 (17), 6054–6066.

Govers, G., Oost, K.V., Wang, Z., 2014. Scratching the critical zone: the global footprint of agricultural soil erosion. Procedia Earth Planet. Sci. 10, 313–318. Geochemistry of the Earth's surface GES-10 Paris France, 18-23 August, 2014.

Guerra, C., Pinto-Correia, T., Metzger, M., 2014. Mapping soil erosion prevention using an ecosystem service modeling framework for integrated land management and policy. Ecosystems 17 (5), 878–889.

Hilker, T., Wulder, M., Coops, N., Seitz, N., White, J., Gao, F., Masek, J., Stenhouse, G., 2009. Generation of dense time series synthetic Landsat data through data blending with MODIS using a spatial and temporal adaptive reflectance fusion model. Remote Sens. Environ. 113 (9), 1988–1999.

Hird, J., McDermid, G., 2009. Noise reduction of NDVI time series: an empirical comparison of selected techniques. Remote Sens. Environ. 113 (1), 248–258.

Houborg, R., Fisher, J., Skidmore, A., 2015. Advances in remote sensing of vegetation function and traits. Int. J. Appl. Earth Obs. Geoinf. 43, 1–6. Special Issue on "Advances in remote sensing of vegetation function and traits".

Huang, B., Zhang, H., 2014. Spatio-temporal reflectance fusion via unmixing: accounting for both phenological and land-cover changes. Int. J. Remote Sens. 35 (16), 6213–6233.

Inan, H., Sagris, V., Devos, W., Milenov, P., van Oosterom, P., Zevenbergen, J., 2010. Data model for the collaboration between land administration systems and agricultural land parcel identification systems. J. Environ. Manag. 91 (12), 2440–2454.

Kandziora, M., Burkhard, B., Müller, F., 2013. Mapping provisioning ecosystem services at the local scale using data of varying spatial and temporal resolution. Ecosyst. Serv. 47–59.

Kaspar, F., Zimmermann, K., Polte-Rudolf, C., 2014. An overview of the phenological observation network and the phenological database of Germany's national meteorological service (Deutscher Wetterdienst). Adv. Sci. Res. 11, 93–99.

Li, X., Zhang, X., Zhang, L., Wu, B., 2014. Rainfall and vegetation coupling index for soil erosion risk mapping. J. Soil Water Conserv. 69, 213–220.

Lobell, D., 2013. The use of satellite data for crop yield gap analysis. Field Crop Res. 143, 56–64.

López-Serrano, P., Corral-Rivas, J., Díaz-Varela, R., Álvarez González, J., López-Sánchez, C., 2016. Evaluation of radiometric and atmospheric correction algorithms for aboveground forest biomass estimation using Landsat 5 TM data. Remote Sens. 8 (5), 369–388.

Masek, J., Vermote, E., Saleous, N., Wolfe, R., Hall, F., Huemmrich, F., Gao, F., Kutler, J., Lim, T., 2006. A Landsat surface reflectance data set for North America 1990–2000. IEEE Geosci. Remote Sens. Lett. 3, 69–72.

Meng, J., Du, X., Wu, B., 2013. Generation of high spatial and temporal resolution NDVI and its application in crop biomass estimation. Int. J. Digital Earth 6 (3), 203–218.

Miller, R., Peter, M., Fluck, A., 2012. Kooperation und nachhaltige Maßnahmen zum Schutz vor Bodenerosion - Ein Praxisbeispiel aus der Wetterau. Bodenschutz 12 (1), 11–15.

Möller, M., Birger, J., Gidudu, A., Gläßer, C., 2013. A framework for the geometric accuracy assessment of classified objects. Int. J. Remote Sens. 34, 8685–8698.

Möller, M., Koschitzki, T., Hartmann, K.-J., Jahn, R., 2012. Plausibility test of conceptual soil maps using relief parameters. CATENA 88 (1), 57–67.

Möller, M., Volk, M., 2015. Effective map scales for soil transport processes and related process domains - statistical and spatial characterization of their scale-specific inaccuracies. Geoderma 247-248, 151–160.

Montaghi, A., Larsen, R., Greve, M., 2013. Accuracy assessment measures for image segmentation goodness of the land parcel identification system (LPIS) in Denmark. Remote Sens. Lett. 4 (10), 946–955.

Olexa, E., Lawrence, R., 2014. Performance and effects of land cover type on synthetic surface reflectance data and NDVI estimates for assessment and monitoring of semi-arid rangeland. Int. J. Appl. Earth Obs. Geoinf. 30, 30–41.

Panagos, P., Borrelli, P., Robinson, D.A., 2015. Common agricultural policy: tackling soil loss across Europe. Nature 526 (7572), 195.

Panagos, P., Karydas, C., Ballabio, C., Gitas, I., 2014a. Seasonal monitoring of soil erosion at regional scale: an application of the G2 model in Crete focusing on agricultural land uses. Int. J. Appl. Earth Obs. Geoinf. Part B 27, 147–155.

Panagos, P., Karydas, C., Gitas, I., Montanarella, L., 2012. Monthly soil erosion monitoring based on remotely sensed biophysical parameters: a case study in Strymonas river basin towards a functional pan-European service. Int. J. Digital Earth 5 (6), 461–487.

Panagos, P., Karydasb, C., Borrellia, P., Ballabioa, C., Meusburger, K., 2014b. Advances in soil erosion modelling through remote sensing data availability at European scale. Proc. SPIE 9229-0I, 1–10.

Prabhakara, K., Hively, W., McCarty, G., 2015. Evaluating the relationship between biomass, percent groundcover and remote sensing indices across six winter cover crop fields in Maryland, United States. Int. J. Appl. Earth Obs. Geoinf. 39, 88–102.

Prasuhn, V., 2011. Soil erosion in the Swiss midlands: results of a 10-year field survey. Geomorphology 126, 32–41.

Prasuhn, V., Liniger, H., Gisler, S., Herweg, K., Candinas, A., Clement, J.-P., 2013. A high-resolution soil erosion risk map of Switzerland as strategic policy support system. Land Use Policy 32, 281–291.

Renard, K., Foster, G., Weesies, G., Porter, J., 1991. RUSLE - revised universal soil loss equation. J. Soil Water Conserv. 46 (3), 30–33.

Renschler, C., 2003. Designing geo-spatial interfaces to scale process models: the GeoWEPP approach. Hydrol. Process. 17, 1005–1017.

Rivera, J., Verrelst, J., Delegido, J., Veroustraete, F., Moreno, J., 2014. On the semi-automatic retrieval of biophysical parameters based on spectral index optimization. Remote Sens. 6 (6), 4927–4951.

Robinson, D., 2015. Changing soil science to understand soil change. Science 526 (6218), 140.

Roo, A.D., Wesseling, C., Ritsema, C., 1996. LISEM: a single event physically-based hydrologic and soil erosion model for drainage basins: I. Theory, input and output. Hydrol. Process. 10 (8), 1107–1117.

Rouse, J., Jr, R.H., Schell, J.A., Deering, D., 1974. Monitoring vegetation systems in the Great Plains with ERTS, NASA SP-351. Third ERTS-1 Symposium. Vol. 1. WNASA, Washington, DC, pp. 309–317.

Routschek, A., Schmidt, J., Enke, W., Deutschlaender, T., 2014a. Future soil erosion risk - results of GIS-based model simulations for a catchment in Saxony/Germany. Geomorphology 206, 299–306.

Routschek, A., Schmidt, J., Kreienkamp, F., 2014b. Impact of climate change on soil erosion - a high-resolution projection on catchment scale until 2100 in Saxony/Germany. Catena 121, 99–109.

Schaaf, C., Gao, F., Strahler, A., Lucht, W., Li, X., Tsang, T., Strugnell, N., Zhang, X., Jin, Y., Muller, J.-P., Lewis, P., Barnsley, M., Hobson, P., Disney, M., Roberts, G., Dunderdale, M., Doll, C., d'Entremont, R., Hu, B., Liang, S., Privette, J., Roy, D., 2002. First operational BRDF, albedo nadir reflectance products from MODIS. Remote Sens. Environ. 83, 135–148. The Moderate Resolution Imaging Spectroradiometer (MODIS): a new generation of Land Surface Monitoring.

Schindewolf, M., Schmidt, J., 2012. Parameterization of the EROSION 2D/3D soil erosion model using a small-scale rainfall simulator and upstream runoff simulation. CATENA 91, 47–55.

Schwertmann, U., Vogl, W., Kainz, M., 1990. Bodenerosion durch Wasser - Vorhersage des Abtrags und Bewertung von Gegenmaßnahmen. 2nd, Ulmer Verlag, Stuttgart.

Spatialreference, 2016. Catalogs of spatial reference systems. Accessed on 9th February 2016

A.F., M., Sulla-Menashe, D., Woodcock, C., 2016. Sources of bias and variability in long-term landsat time series over Canadian boreal forests. Remote Sens. Environ. 177, 206–219.

Symeonakis, E., Drake, N., 2010. 10-Daily soil erosion modelling over sub-Saharan Africa. Environ. Monit. Assess. 161 (1), 369–387.

Tian, F., Wang, Y., Fensholt, R., Wang, K., Zhang, L., Huang, Y., 2013. Mapping and evaluation of NDVI trends from synthetic time series obtained by blending Landsat and MODIS data around a coalfield on the loess plateau. Remote Sens. 5 (9), 4255.

Trimble, 2011. eCognition Developer 8.7 reference book. Tech. Rep., Trimble Germany GmbH, Munich, Germany.

Tucker, C., 1979. Red and photographic infrared linear combinations for monitoring vegetation. Remote Sens. Environ. 8, 127–150.

Tyc, G., Tulip, J., Schulten, D., Krischke, M., Oxfort, M., 2005. The RapidEye mission design. Acta Astronaut. 56, 213–219.

Valero, S., Morin, D., Inglada, J., Sepulcre, G., Arias, M., Hagolle, O., Dedieu, G., Bontemps, S., Defourny, P., Koetz, B., 2016. Production of a dynamic cropland mask by processing remote sensing image series at high temporal and spatial resolutions. Remote Sens. 8 (1), 55–76.

Van der Knijff, J., Jones, R., Montanarella, L., 1999. Soil erosion risk in Italy. Tech. Rep., European Soil Bureau, Joint Research Centre, Luxembourg. eUR19022 EN

Vermote, E., Roger, J., Ray, J., 2015. MODIS surface reflectance user's guide - collection 6. Tech. Rep. Version 1.4, NASA GSFC Terrestrial Information Systems Laboratory, MODIS Land Surface Reflectance Science Computing Facility, Greenbelt, USA.

Verrelst, J., Munoz, J., Alonso, L., Delegido, J., Rivera, J.P., Camps-Valls, G., Moreno, J., 2012. Machine learning regression algorithms for biophysical parameter retrieval: opportunities for sentinel-2 and -3. Remote Sens. Environ. 118, 127–139.

Volk, M., Möller, M., Wurbs, D., 2010. A pragmatic approach for soil erosion risk assessment within policy hierarchies. Land Use Policy 27, 997–1009.

Vrieling, A., de Jong, S.M., Sterk, G., Rodrigues, S.C., 2008. Timing of erosion and satellite data: a multi-resolution approach to soil erosion risk mapping. Int. J. Appl. Earth Obs. Geoinf. 10, 267–281.

Vrieling, A., Hoedjes, J.C., van der Velde, M., 2014. Towards large-scale monitoring of soil erosion in Africa: accounting for the dynamics of rainfall erosivity. Glob. Planet. Chang. 115, 33–43.

Walker, J., de Beurs, K., Wynne, R., Gao, F., 2012. Evaluation of Landsat and MODIS data fusion products for analysis of dryland forest phenology. Remote Sens. Environ. 117, 381–393. Remote Sensing of Urban Environments.

Watts, J., Powell, S., Lawrence, R., Hilker, T., 2011. Improved classification of conservation tillage adoption using high temporal and synthetic satellite imagery. Remote Sens. Environ. 115 (1), 66–75.

Wenwen, C., Jinling, S., Jindi, W., Zhiqiang, X., 2012. High spatial-and temporal-resolution NDVI produced by the assimilation of MODIS and HJ-1 data. Can. J. Remote. Sens. 37 (6). (612–327).

Whitcraft, A., Vermote, E., Becker-Reshef, I., Justice, C., 2015. Cloud cover throughout the agricultural growing season: impacts on passive optical earth observations. Remote Sens. Environ. 156, 438–447.

Wischmeier, W., Smith, D., 1962. Soil loss estimation as a tool in soil and water management planning. Bull. Int. Assoc. Sci. Hydrol. 59, 148–159.

Wu, M., Zhang, X., Huang, W., Niu, Z., Wang, C., Li, W., Hao, P., 2015. Reconstruction of daily 30 m data from HJ CCD, GF-1 WFV, Landsat, and MODIS data for crop monitoring. Remote Sens. 7 (12), 16293–16314.

Yang, G., Pu, R., Zhang, J., Zhao, C., Feng, H., Wang, J., 2013. Remote sensing of seasonal variability of fractional vegetation cover and its object-based spatial pattern analysis over mountain areas. ISPRS J. Photogramm. Remote Sens. 77, 79–93.

Zhang, H., Huang, B., Zhang, M., Cao, K., Yu, L., 2015. A generalization of spatial and temporal fusion methods for remotely sensed surface parameters. Int. J. Remote Sens. 36 (17), 4411–4445.

Zheng, B., Campbell, J.B., Serbin, G., Galbraith, J.M., 2014. Remote sensing of crop residue and tillage practices: present capabilities and future prospects. Soil Tillage Res. 138, 26–34.

Zhu, X., Chen, J., Gao, F., Chen, X., Masek, J., 2010. An enhanced spatial and temporal adaptive reflectance fusion model for complex heterogeneous regions. Remote Sens. Environ. 114 (11), 2610–2623.

Zhu, Z., Wang, S., Woodcock, C., 2015. Improvement and expansion of the Fmask algorithm: cloud, cloud shadow, and snow detection for Landsat 4–7, 8, and Sentinel 2 images. Remote Sens. Environ. 159, 269–277.

Zhu, Z., Woodcock, C., 2012. Object-based cloud and cloud shadow detection in Landsat imagery. Remote Sens. Environ. 118, 83–94.